Volume 3
Number 4
April 2024
Pages 481–710

Sensors & Diagnostics

rsc.li/sensors

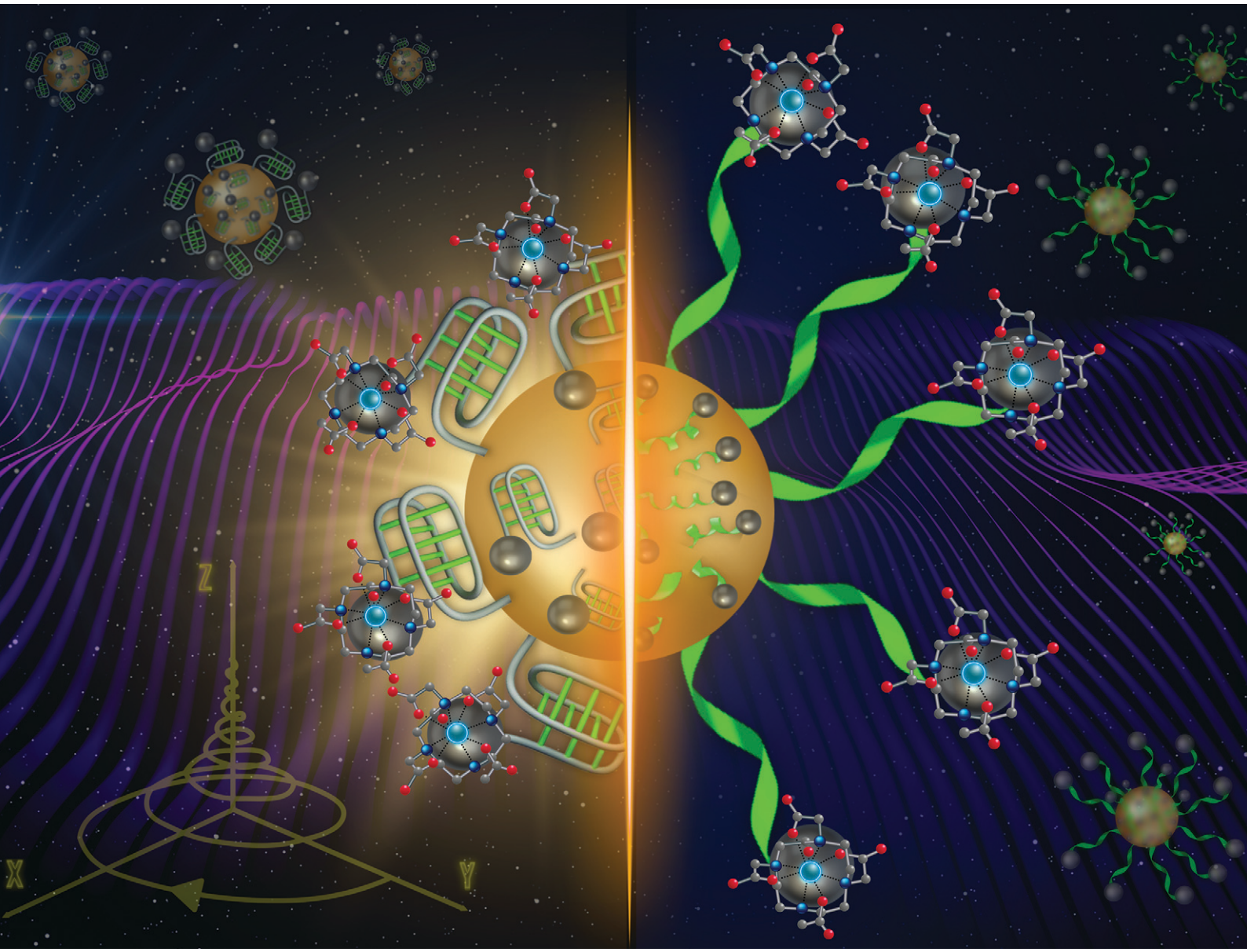

ISSN 2635-0998

ROYAL SOCIETY OF CHEMISTRY

PAPER
Heather A. Clark *et al.*
pH-responsive i-motif-conjugated nanoparticles for MRI analysis

Sensors & Diagnostics

PAPER

View Article Online
View Journal | View Issue

Cite this: *Sens. Diagn.*, 2024, **3**, 623

pH-responsive i-motif-conjugated nanoparticles for MRI analysis†

Kristine Y. Ma, [ab] Mireia Perera-Gonzalez, [b] Nicole I. Langlois, [c] Owen M. Alzubi,[a] Joseph D. Guimond, [a] Chris A. Flask [d] and Heather A. Clark *[a]

Received 26th October 2023,
Accepted 21st February 2024

DOI: 10.1039/d3sd00285c

rsc.li/sensors

Gadolinium (Gd)-based contrast agents (CAs) are widely used to enhance anatomical details in magnetic resonance imaging (MRI). Significant research has expanded the field of CAs into bioresponsive CAs by modulating the signal to image and monitor biochemical processes, such as pH. In this work, we introduce the modular, dynamic actuation mechanism of DNA-based nanostructures as a new way to modulate the MRI signal based on the rotational correlation time, τ_R. We combined a pH-responsive oligonucleotide (i-motif) and a clinical standard CA (Gd-DOTA) to develop a pH-responsive MRI CA. The i-motif folds into a quadruplex under acidic conditions and was incorporated onto gold nanoparticles (iM-GNP) to achieve increased relaxivity, r_1, compared to the unbound i-motif. *In vitro*, iM-GNP resulted in a significant increase in r_1 over a decreasing pH range (7.5–4.5) with a calculated pK_a = 5.88 ± 0.01 and a 16.7% change per 0.1 pH unit. In comparison, a control CA with a non-responsive DNA strand (T_{33}-GNP) did not show a significant change in r_1 over the same pH range. The iM-GNP was further evaluated in 20% human serum and demonstrated a 28.14 ± 11.2% increase in signal from neutral pH to acidic pH. This approach paves a path for novel programmable, dynamic DNA-based complexes for τ_R-modulated bioresponsive MRI CAs.

Introduction

Magnetic resonance imaging (MRI) offers multiple advantages as an anatomical imaging technique including deep tissue penetration, minimal invasiveness, and 3D scanning capabilities. Traditionally, paramagnetic metal-based contrast agents (CAs) have been used to improve imaging resolution for enhanced structural and functional details. Recent advances in the field have led to the development of bioresponsive MRI CAs, which offer new strategies for achieving biomarker detection and molecular imaging[1] by responding to a physiological trigger. To achieve bioresponsive modulation of MRI signals ("relaxivity"), several strategies can be used to tune the properties of paramagnetic metal-based CAs. One popular approach is to alter the hydration state (q), which refers to the number of water molecules directly coordinated to the metal center of a coordinate complex.[2] Some examples of q-modulated MRI CAs include different chelate complexes that respond to enzymatic cleaveage,[3,4] cations (*e.g.*, zinc,[5] calcium,[6–8] copper,[9–11] and mercury[12]), pH,[13] and oxidation reactions.[14,15] While CAs featuring q-modulation have paved the way for bioresponsive MR imaging, issues with thermodynamic instability,[16] metal displacement by coordinating anions *in vivo*,[17] and synthetic inefficiency (*i.e.* laborious purification procedures) present challenges for the development of new CAs for MR imaging in complex systems. Additional methods to modulate the signal of a CA without depending on q-modulation have the potential to unlock new avenues for bioresponsive imaging.

Enhancement of relaxivity can be alternatively attained by increasing the molecular weight of a CA by incorporating paramagnetic metal chelates onto a nanosized platform. This increase in CA size slows down the rotation of CA described by the rotational correlation time, τ_R.[18] In our previous works, we have demonstrated this phenomenon by developing nanoplatforms that are simultaneously modulated by q and τ_R parameters. We paired q-modulated pH-responsive CAs with enzymes on a nanoparticle to demonstrate acetylcholine imaging in a rat brain.[19] The pH-sensing mechanism of this CA, Gd(NP-DO3A),[20] was dependent on changing the protonation state of the nitrophenol arm of the ligand, which consequently changes q (q = 1 *vs.* q = 2). Using the same pH-responsive Gd-based CA, we developed a DNA-dendrimer-based MRI CA that demonstrated a significant increase in relaxivity for use in quantitative pH measurement.[21]

[a] *School of Biological and Health Systems Engineering, Arizona State University, Tempe AZ, USA. E-mail: Heather.Ann.Clark@asu.edu*
[b] *Dept. of Bioengineering, Northeastern University, Boston MA, USA*
[c] *Dept. of Chemistry and Chemical Biology, Northeastern University, Boston MA, USA*
[d] *Depts. of Radiology, Biomedical Engineering, and Pediatrics, Case Western Reserve University, Cleveland OH, USA*

† Electronic supplementary information (ESI) available. See DOI: https://doi.org/10.1039/d3sd00285c

Building from our previous works, we engineered a pH-responsive CA based on τ_R-modulation that is independent of *q*-modulation. We paired the FDA-approved Gd-DOTA (Dotarem®) CA with a stimuli-responsive DNA i-motif oligonucleotide. The i-motif is one of the simplest dynamic DNA structures that can be programmed to reversibly respond to a specific stimulus, in this case – pH.[22] In acidic environments, hemiprotonation of cytidine bases in the i-motif sequence induces a strand conformational change through folding, forming a series of intercalated cytidine–cytidine+ base pairs in a quadruplex secondary structure.[23] This folding process increases the rigidity of the complex, thus slowing the τ_R relative to the unfolded linear structure, resulting in an increase in relaxivity (r_1). The rate of water exchange between the inner-sphere and bulk solvent, $k_{ex} = 1/\tau_M$, is another parameter that can be modulated for designing bioresponsive CAs. While modulating τ_M is a complex process that is beyond the scope of this work, the i-motif folding mechanism can potentially impact water access to the CA and thus affect the MRI signal as well.

In this work, we coupled Gd-DOTA onto an i-motif sequence[24] for a novel pH-responsive DNA-based CA design. The i-motif coupled with Gd-DOTA was loaded onto a gold nanoparticle (GNP) to expand the size of the complex and further increase MRI signals by slowing τ_R. The GNP and size were chosen as a platform to load the pH-responsive CA as it has been widely reported in the literature with established protocols for loading DNA,[25,26] and for use as a biosensor platform *in vivo*.[27] We demonstrated that our pH-responsive i-motif conjugated GNP (iM-GNP) can increase MRI signals (r_1) through a bioresponsive mechanism, compared to a non-responsive control composed of a 33 nt repeating thymine oligonucleotide (T_{33}-GNP) which does not fold in response to pH changes. Over traditional "on–off" MRI responsive systems, our approach features reversibility, tunability and high sensitivity over a physiologically-relevant pH range. Our approach is of special interest for paving a path for engineering novel applications of programmable dynamic DNA-based complexes for non *q*-modulated bioresponsive CAs for MR imaging.

Experimental methods

Gd-DOTA & oligonucleotide coupling preparation

Custom amine/thiol-functionalized single-strand DNA oligonucleotides were purchased from MilliporeSigma, with sequences reported in Table S1.† The concentration of DNA was determined *via* the absorbance at 260 nm, ε = 282.8 mM^{-1} cm^{-1} for the i-motif strand and ε = 267.9 mM^{-1} cm^{-1} for the control T_{33} strand. Gd-DOTA was conjugated onto the DNA oligonucleotide *via* thioamide coupling on the amine terminal end of the DNA oligonucleotide. Gd–*p*-SCN-Bn-DOTA (2.46 mg, 3 μmol, macrocyclics) and the amine/thiol-functionalized DNA oligonucleotide (0.02 μmol) were dissolved in 0.5 mL of 0.1 M carbonate buffer and incubated for 20 h at room temperature. DNA–Gd-DOTA conjugates were purified with ethanol precipitation followed by an Illustra NAP-10 column (GE Health) to remove excess Gd–*p*-SCN-Bn-DOTA. The conjugates were eluted in nanopure water and then lyophilized overnight (Labconco).

Analysis of Gd-DOTA coupling to DNA by HPLC

Chromatographic analyses were performed using an Agilent 1260 Infinity II HPLC System, equipped with a vial sampler, quaternary pump, wide-range diode array detector, and ChemStation software. A method for the separation of free DNA from Gd-DOTA conjugates was developed using ion-paired reversed phase chromatography on a Zorbax EclipsePlus C18 column (4.6 mm × 250 mm, 5 μm, Agilent). Mobile phase A was 50 mM triethylammonium acetate (TEAA, pH 7.0), with acetonitrile as mobile phase B. Samples of unpurified DNA–Gd-DOTA conjugates were reduced with 0.1 M tris(2-carboxyethyl)phosphine (TCEP) for 1 h, diluted in the mobile phase, and then analyzed at a flow rate of 0.65 mL min^{-1} using a gradient elution method (10–30% B over 20 min). Unmodified DNA samples were diluted in the mobile phase and analyzed using the same gradient method for comparison. The online absorbance signal for the DNA was monitored at 260 nm. The retention times of the i-motif strand, iM–Gd-DOTA, the T_{33} strand, and T_{33}–Gd-DOTA were 9.15 min, 9.44 min, 9.81 min, and 10.26 min, respectively. Residual Gd–*p*-SCN-Bn-DOTA present in the samples exhibited peaks with retention times of 9.85 min, 10.58 min, 11.15 min, 11.80 min, and 11.98 min. Disulfide dimers present in the non-reduced, unreacted DNA samples exhibited peaks with retention times of 10.05 min and 10.60 min for the i-motif and T_{33} strands.

Preparation of Gd-DOTA oligonucleotide functionalized gold nanoparticles

Oligo-functionalized gold nanoparticles (GNPs) (10 nm) were prepared according to literature procedures.[25] Briefly, the Gd-DOTA-conjugated i-motif and T_{33} oligos (0.02 μmol) were resuspended in a solution of 0.1 M tris(2-carboxyethyl) phosphine (TCEP) (5.73 mg, 20 μmol) and 0.1 M phosphate buffer (PB) at pH 8 to reduce the disulfide bonds at the terminal thiol ends of the oligonucleotides. After 1 h in the reducing environment, the freshly deprotected oligos (4 nmol) were diluted in nanopure water (250 μL) and then added to 1 mL of gold colloid (10 nM, Sigma-Aldrich) in an Eppendorf tube. The solution was shaken for 2 h prior to salt stabilization. iM-GNP and T_{33}-GNP were buffered to a pH of 7.2 with a final concentration of 10 mM PB and 0.01% SDS. After 30 min equilibration, samples were salt aged with NaCl solution, slowly increasing the NaCl concentration to 1.0 M over a 4 h period. GNPs were sonicated during this salt aging process. Particles were shaken overnight to yield fully functionalized GNPs. Removal of any unbound oligonucleotides was performed by washing through sequential centrifugation steps (10 kDa MWCO, 4000 × *g*, 20 °C), supernatant removal, and resuspension (0.1% SDS in

water). This procedure was repeated four times. To determine the concentration of each GNP sample, we used the reported extinction coefficient at Abs = 530 nm for 10 nm particles: $\varepsilon = 1.06 \times 10^8\ M^{-1}\ cm^{-1}$.

pH titration (1.4 T NMR)

iM-GNP and T_{33}-GNP (30 nM) were dispersed in 20 mM MES/HEPPS/HEPES at pH = 9. The pH titration was carried out by adding 1–3 μL increments of 0.1 M HCl. With each addition, the solution was vigorously vortexed, the pH was measured using a calibrated pH meter (Orion Star™), and T_1 measurements were obtained using a 1.4 T Bruker minispec mq60 NMR analyzer (60 MHz, Bruker Inc., Billerica, MA) at 37 °C. The relaxivity (r_1) at each point was calculated with the GNP concentration. The gain was set to 56 dB and T_1 delays of 6–8000 ms were used. Four T_1 replicate measurements were performed, with the last three being averaged to stabilize the temperature effect on the measurement. T_1 values were measured in the pH range of 4.5–7.5. Relaxivity values were obtained by using eqn (1) and plotted against pH, fitted to a dose–response curve.

$$r_i = \frac{\frac{1}{T_i} - \frac{1}{T_{i,0}}}{[\mathrm{CA}]} \quad (1)$$

Eqn (1): $T_i = T_1$ measurement of CA, $T_{i,0} = T_1$ measurement of the buffer solution, and [CA] = concentration of GNPs.

Relaxivity analysis (3.0 T MRI)

The T_1 maps were calculated on a voxel-by-voxel basis by three-parameter fitting of eqn (2) to the signal intensity images at each TR.

$$M_z(T_R) = M_o \cdot (1 - e^{-T_R/T_1}) + C \quad (2)$$

where M_z = longitudinal magnetization, T_R = repetition time, M_o = equilibrium signal magnetization, C = constant, and T_1 = longitudinal relaxation rate constant.

Regions of interest (ROI) were manually defined from the MR signal intensity images for each capillary tube. The resulting T_1 values were averaged over each ROI. Relaxivity values (r_i) were obtained from eqn (2), where T_1 = longitudinal relaxation of the CA in buffer.

Cell viability by MTT assay

Cell viability was determined using the 3-(4,5-dimethylthiazol-2-yl)-2,5-diphenyltetrazolium bromide reduction (MTT) assay. HEK293T cells were seeded in 96-well plates at a density of 2.5×10^4 cells in 100 μL of cell media per well. After 24 h incubation (37 °C, 5% CO_2), cells were treated with water-soluble iM-GNP by adding 50 μL of various concentrations for final working concentrations (0 nM to 20 nM). After 24 h exposure and incubation, media in wells were carefully replaced with 200 μL of MTT–DMEM (0.2 mg mL^{-1}). Cells were incubated for 3 h and media were carefully replaced with 100 μL of dimethyl sulfoxide (DMSO). After 15 min of shaking at room temperature, the absorbance was measured at 540 nm with a BioTek Synergy H1 microplate reader. The viability was assessed by a percentage with respect to controls (set as 100%).

Cell viability by NR assay

The cell viability was determined using the neutral red (NR) uptake assay. HEK293T cells were seeded in 96-well plates at a density of 2.5×10^4 cells in 100 μL of cell media per well. After 24 h incubation (37 °C, 5% CO_2), cells were treated with water-soluble iM-GNP by adding 50 μL of various concentrations for final working concentrations (0 nM to 20 nM). After 24 h exposure and incubation, media in wells were carefully replaced with 100 μL neutral red medium (50 μg mL^{-1}). Cells were incubated for 2 h. Media were carefully replaced with 150 μL of phosphate buffered saline (PBS) and centrifuged (1000 × g, 20 °C) for 10 min. Media were carefully removed, and the cell pellet was resuspended in 150 μL of neutral red destain solution (50% ethanol, 1% glacial acetic acid). After 10 min of shaking at room temperature, the absorbance was measured at 540 nm with a BioTek Synergy H1 microplate reader.

Cell viability analysis

The viability was assessed by a percentage with respect to controls (0 nM, set as 100%) depicted by eqn (3). Values were corrected with blanks. The statistical significance was assessed by one-way analysis of variance (ANOVA).

$$\%\ \mathrm{Viability} = \frac{\mathrm{Mean\ OD_{Sample}}}{\mathrm{Mean\ OD_{Control}}} \times 100 \quad (3)$$

Results & discussion

To prepare our CAs, Gd-DOTA was conjugated onto the DNA i-motif sequence, purified, and validated before loading onto GNPs. By using commercially-available Gd-DOTA, the need for chelating Gd as a separate step during synthesis is eliminated, thus preventing non-specific interactions of Gd^{3+} to the DNA.[28] To tailor the sensor for actuation in a relevant dynamic range, we chose a reported i-motif sequence which undergoes a change in folding from 5 to 95% between pH 6.26 and 5.9.[24] This range is useful in the study of disease states such as metastatic tumors (pH 6.1–6.4 (ref. 29)) or tissue acidosis (pH 6.0–7.0 (ref. 30)). A 12 nt length spacer of thymine bases was chosen to maintain an ~4 nm distance between the GNP surface and the i-motif strand to provide flexibility and freedom[31] for the i-motif to fold and unfold by minimizing electrostatic repulsions with the GNP surface. We also prepared a control group using repeating thymine residues with the same number of base pairs (T_{33}) as the i-motif with the spacer. The 5′ end of each oligo was amine-

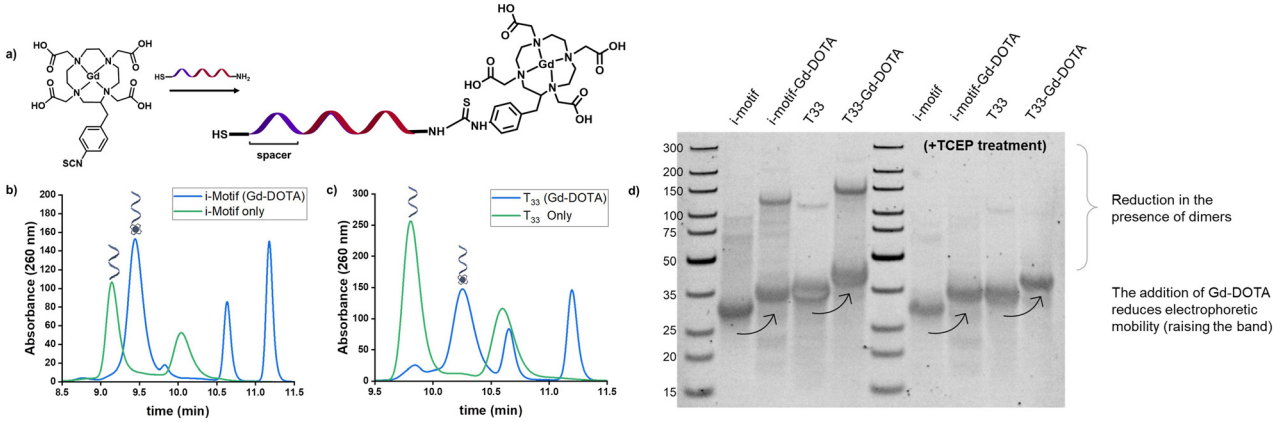

Fig. 1 Scheme of pH-responsive i-motif with Gd-DOTA and HPLC characterization. a) Conjugation of Gd–*p*-SCN-Bn-DOTA to the DNA oligonucleotides was performed *via* thioamide coupling. Ion-paired reversed phase HPLC demonstrates successful conjugation of Gd-DOTA to DNA oligonucleotides. b) i-Motif oligonucleotide sequence (green) *vs.* i-motif oligonucleotide conjugated with Gd-DOTA (blue). Successful coupling of Gd-DOTA is indicated by a retention time shift of 0.30 min. c) Control, T_{33}, oligonucleotide sequence (green) *vs.* T_{33} oligonucleotide conjugated with Gd-DOTA (blue). Successful coupling of Gd-DOTA is indicated by a retention time shift of 0.45 min. In the DNA only samples, the secondary peak is attributed to non-reduced disulfide dimers, while the additional peaks in the product samples are consistent with residual Gd–*p*-SCN-Bn-DOTA. d) Native PAGE characterization of Gd-DOTA coupling to the DNA strands. From left to right: ladder, i-motif oligonucleotide, i-motif + Gd-DOTA, T_{33} oligonucleotide, T_{33} + Gd-DOTA, ladder, TCEP treated i-motif oligonucleotide, TCEP treated i-motif + Gd-DOTA, TCEP treated T_{33} oligonucleotide, TCEP treated T_{33} + Gd-DOTA. After running, the gel was stained with 1× GelRed® DNA staining solution.

modified for coupling to Gd-DOTA, and the 3′ end was thiol-modified for GNP attachment. With a commonly used primary amine reaction, we coupled the isothiocyanate-functionalized Gd-DOTA with the amine end of the DNA through a thioamide linkage (Fig. 1a). Upon purification and reduction of the disulfide bonds *via* TCEP, successful coupling of the Gd-DOTA was validated by ion-paired reverse-phase liquid chromatography, as evidenced by shifts to later retention times compared to the unmodified oligonucleotide strands (Fig. 1b and c). Peaks from the unmodified i-motif/T_{33} strands were not observed in the chromatograms after the modifications, indicating a high reaction conversion (DNA : Gd-DOTA ≈ 1 : 1 ratio). Residual Gd–*p*-SCN-Bn-DOTA in the reacted samples contributed to additional peaks in the chromatogram as shown in Fig. S1.† Additionally, in the non-reduced reference DNA strands, a secondary peak was observed at later retention times that is consistent with the presence of disulfide dimers compared to the reduced single strands. These results were further validated through gel electrophoresis (Fig. 2d) where it can be observed that a reduced electrophoretic mobility is associated with Gd-DOTA modification on the strands and that TCEP treatment significantly reduced the observation of disulfide dimers present in the samples.

The Gd-DOTA-conjugated i-motif and T_{33} control were loaded onto GNPs following established protocols[25,26] for maximal DNA loading per GNP (Fig. 2a–c). Salt aging decreases the electrostatic interaction between neighboring oligonucleotides and thus improves the loading efficiency of the DNA on the surface of the GNP. To remove the unbound DNA, sequential centrifugation, supernatant removal, and resuspension (0.01% SDS in water) were performed and repeated. The unbound DNA in the sample is completely removed after at least three washes as confirmed by both agarose gel electrophoresis[32] (Fig. 2e) and ICP-MS (Fig. S3†).

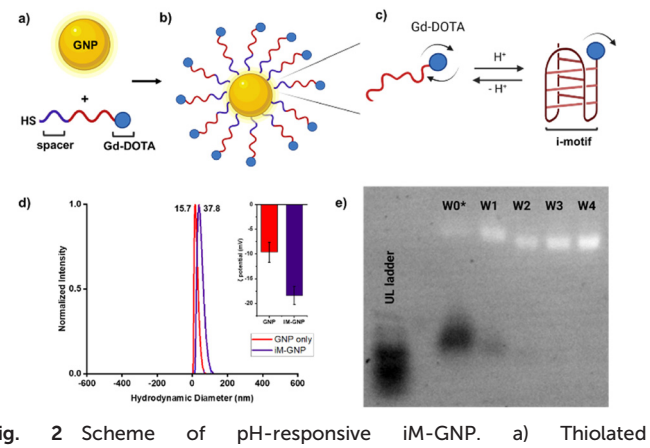

Fig. 2 Scheme of pH-responsive iM-GNP. a) Thiolated oligonucleotides were loaded onto GNP after TCEP treatment b) iM-GNP in the fully expanded form at basic pH. c) Folding of the i-motif oligonucleotides occurs in the presence of increased H^+. d) DLS analysis shows that the average size of unmodified commercial 10 nm GNP was 15.7 nm, while iM-GNP had a larger average size of 37.8 nm. Inset shows the ζ potential of the unmodified GNP = −9.7 ± 2.0 mV and iM-GNP = −18.4 ± 1.8 mV. e) Electrophoretic mobility of iM-GNP (2.0% agarose gel, 1× TAE). The first lane (from left to right) corresponds to the ultralow ladder. W0* is the iM-GNP reaction solution before washing. W1, W2, W3, and W4 represent the iM-GNP concentrate after 1, 2, 3, and 4 washes, respectively. It appears that after at least 3 washes, there is no free DNA (black bands) and the iM-GNP sensor (white bands) is no longer changing the size/charge due to non-covalently bound DNA. This is further validated by ICP-MS analysis (Fig. S3†).

The zeta potential of the GNPs increased in magnitude after DNA loading (unmodified GNP = −9.7 ± 2.0 mV and iM-GNP = −18.4 ± 1.8 mV), which indicated successful gold–thiol linkage and DNA immobilization onto the GNP (Fig. 2d). This increase in negative surface charge is consistent with observations in previous reports for DNA immobilization on the surface of GNPs.[33] The gadolinium content was estimated using ICP analysis, yielding 123.5 ± 30.4 units of oligo–Gd-DOTA per GNP. DLS was used to measure the average diameter of iM-GNP (37.8 nm) in comparison to unmodified GNPs (15.7 nm) (Fig. 2d). The increase in hydrodynamic size of the NP can be attributed to the immobilization of the DNA on the surface, further corroborating successful functionalization to yield the iM-GNP (Fig. S2†).

We characterized the pH-responsive properties of the iM-GNP and the control, T_{33}-GNP, using both the benchtop 1.4 T NMR and the preclinical 3.0 T MRI scanner. From the 1.4 T NMR at 37 °C, the relaxivity profiles of iM-GNP as a function of pH were obtained between pH 4.50 and 7.50 with a calculated pK_a of 5.88 ± 0.01 and a 16.7% change per 0.10 pH unit (Fig. 3a). These measured values are lower than the reported pK_a of the i-motif strand (6.26 ± 0.01 at 25 °C).[24] We hypothesize that this slight shift in observed pK_a can be attributed to factors including modification of the sequence with additional thymine bases as a spacer, the coupling of the DNA with Gd-DOTA as the reporter, and differences in buffer and instrument conditions. The per metal-center magnetic relaxivity measured at 1.4 T for iM-GNP was approximated by accounting for the ICP-MS measured 123 Gd-DOTA sites per GNP: acidic (pH = 5) r_1 = 60.7 ± 1.1 mM^{-1} s^{-1} and neutral (pH = 7) r_1 = 47.1 ± 1.7 mM^{-1} s^{-1} (n = 3). The per metal center relaxivities resulted in significantly higher values compared to the standard Gd-DOTA agent (~3.11 mM^{-1} s^{-1} at 1.4 T).[34] When comparing the percent change in r_1 between iM-GNP and T_{33}-GNP, there is a clear increase in signal change for iM-GNP (Fig. 3b). The iM-GNP signal enhancement is also significantly greater than the Gd-DOTA conjugated i-motif strand alone, which exhibited a per-metal center relaxivity of 48.8 mM^{-1} s^{-1} at pH 5 (Fig. S5†).

In addition to τ_R, the folding of the i-motif can contribute to reduced water activity due to an ordered layer of water on the surface caused by nanoconfinement conditions.[35] The restricted space makes the water molecules more ordered than in the bulk solution affecting τ_M and thus affecting relaxivity.[35] Water molecules in enclosed environments have a considerably different diffusion than in the bulk, which leads to increased relaxivities.[36] Previous works showed that introducing steric constraints on the water-binding site[37,38] increases the water exchange rate and thus contributes to increased relaxivity. Under confined conditions, the strong outer sphere relaxation from the i-motif could be the influencing τ_M properties of the Gd-DOTA. Understanding the degree of impact of τ_M from folding and unfolding of the i-motif coupled with the MR CA is outside the scope of this work but could be a subject of future studies. For the control, T_{33}-GNP, there was no significant change in r_1 *in vitro* at 1.4 T over the pH range of 4.50–7.50 (Fig. S4†). When comparing the percent change in r_1 between iM-GNP and T_{33}-GNP, there is a clear increase in signal change for iM-GNP (Fig. 3b).

The change in MR response was also characterized using the 3.0 T MRI. We expected that the relaxivity profiles from 3.0 T would exhibit similar trends to the data obtained from 1.4 T, with a slight downward intensity shift in the pH-relaxivity curve due to the increase in magnetic field strength.[39] We prepared 30 nM iM-GNP (n = 3) in solutions of increasing pH buffers (pH 5.00, 5.50, 5.75, 6.00, and 7.00) to capture the change in relaxivity as a function of pH. Using an in-house developed MRI testbed for small volume analysis (Fig. S6†), we observed a significant change in signal between pH 5.0 and 7.0, $\Delta 1/T_1$ 28.6 ± 7.4% with a calculated pK_a of 5.86 ± 0.14 and a 12.7% change per 0.10 pH unit (Fig. 3c). The raw plots for the 3.0 T MRI signal intensity over repetition time were used to calculate the iM-GNP T_1 values and are reported in (Fig. S7†).

To demonstrate the suitability of the application of iM-GNP in complex biological environments, we prepared 20% human serum (HS) in pH 4.99 buffer and pH 8.79 buffer. There was a measurable signal change between the basic pH condition and the acidic pH condition of 28.14 ± 11.2% (n = 2). Our results suggest that the i-motif can fold not only *in vitro* under well-controlled conditions, but also in a complex medium. Previous reports show that various media conditions (*i.e.*, water, plasma, blood) do not impact the r_1 signal of the Gd-based CA significantly,[41] and that the folding capabilities of the i-motif are not hindered in complex *in vivo* environments (*i.e.*, pH-responsive nanomachine[42]).

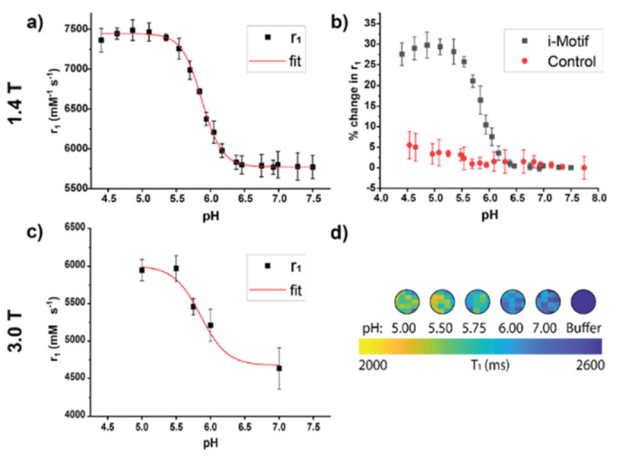

Fig. 3 Relaxivity profiles of the 30 nM CA across different pH values measured using a 1.4 T NMR (37 °C) and a 3.0 T MRI (25 °C). a) Relaxivity profile of iM-GNP in MES/HEPPS/HEPES as a function of pH at 1.4 T. Relaxivity (r_1) was calculated from the GNP concentration from titration experiments, error bars indicate standard deviation, n = 3. b) Comparison of iM-GNP and T_{33}-GNP relaxivity over pH plotted as % change in r_1. c) Plot of measured r_1 values from the *in vitro* MRI color map at different pH values, error bars indicate standard deviation, n = 3. d) Representative image of ROIs from a T_1 color map of the *in vitro* test bed using a 3.0 T MRI.

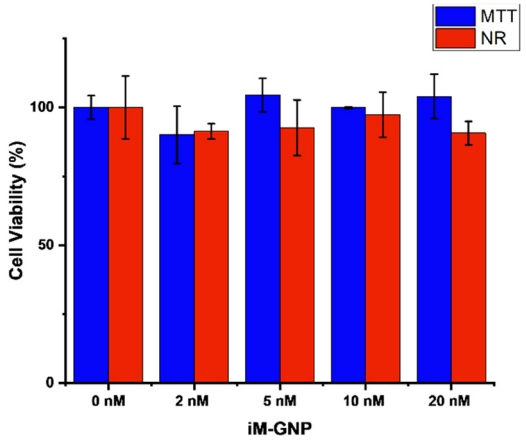

Fig. 4 MTT and neutral red (NR) assays for HEK293T viability after treatment of iM-GNP. Viability measured after 24 h treatment of 0 nM (MTT: 100% ± 4.2%, NR: 100% ± 11.4%), 2 nM (MTT: 90.2% ± 10.4%, NR: 91.0% ± 2.8%), 5 nM (MTT: 104.5% ± 6.1%, NR: 92.6% ± 10.1%), 10 nM (MTT: 99.9% ± 0.3%, NR: 97.3% ± 8.2%), and 20 nM (MTT: 104.0% ± 8.1%, NR: 90.6% ± 4.3%) iM-GNP concentrations. Error bars indicate standard deviation, n = 3. One-way analysis of variance (ANOVA) was performed for MTT (p = 0.14) and NR (p = 0.57) cell viabilities. No significance was observed ($p > 0.05$).

We evaluated the potential toxicity of the iM-GNP with two different *in vitro* cell viability assays. MTT and NR assays were applied to iM-GNP treated HEK293T cells to examine biocompatibility and safety. Both assays are commonly used for investigating the cell viability of drugs, chemical exposure, and nanoparticles.[40] Our ANOVA analysis from MTT (p = 0.14) and NR (p = 0.57) assays depict no significant differences ($p > 0.05$) between the control and different iM-GNP concentration treatment groups (Fig. 4), indicating the iM-GNP's biocompatibility.

A significant advantage in using the i-motif as the MR signal modulating element is the ease of tunability of the i-motif response range by making changes in the DNA sequence. The i-motif based system can be modified by using various cytosine derivatives and by extending the length of the C–C+ strands to tune the pH range by +0.14 and −0.22 pH units in addition to the folding kinetics.[24]

Future work could address several research avenues that would improve the quantitative aspects of this study. First, there is an observed drop in signal for both the acidic and neutral group when measuring the iM-GNP in 20% HS over an extended period of time at 37 °C (Fig. S8†). Enzymatic destabilization from digestion by nucleases present in HS is likely the source of DNA structural instability, causing the i-motif to lose function overtime. Future adaptations of this work could investigate ways to stabilize the i-motif against degradation by introducing alternative materials (*e.g.* PS-DNA, LNA, other XNAs).[43]

Second, future studies could investigate the optimal balance between CA size and CA homogeneity (*i.e.* same number of Gd–CA per DNA nanostructure[21]) without compromising the potential for accurate pH quantification. This is because accurate pH quantification for this study is hindered by the inhomogeneity of Gd attachments to each nanoparticle complex; however, the use of GNPs enabled dense packing of Gd-DOTA onto a single platform to maximize the signal. Third, potential studies can also include quantifying pH independent of CA concentration, by using a second non-pH-responsive CA with the same concentration in tandem with the iM–CA, as in our previously reported work.[21] This second CA could be: 1) a T_2-modulated CA (using dual contrast MR fingerprinting[44]); 2) a 19F or 13C based CA (using multi-nuclear MRI);[45] and/or 3) a radiolabeled agent (using PET/MRI).[46] In summary, the desirable characteristics of the pH-responsive i-motif-conjugated NPs for MR analysis enable another step towards translation of more bioresponsive CAs into future *in vivo* studies.

Conclusions

We have presented a τ_R-modulated bioresponsive CA based on the actuation mechanism of the i-motif for imaging pH using MRI. The pH-responsiveness was demonstrated by 1.4 T relaxometer analysis with a measured pK_a of 5.88 ± 0.01 and a 16.7% change per 0.10 pH unit, with similar results to 3.0 T MRI analysis. As a platform, the iM-GNP demonstrated robust MR signals with a 1.4 T measured per-metal center relaxivity of r_1 = 60.7 ± 1.1 mM^{-1} s^{-1} at acidic pH, a 20-fold increase compared to Gd-DOTA alone. This MR CA demonstrated a significant change in signal *in vitro* compared to the non-responsive T_{33}-GNP control particles. Upon analysis of both particles in 20% HS under acidic and neutral conditions, the iM-GNP demonstrated a significant change in signal of 28.14 ± 11.2%. The iM-GNP's mechanism is not only effective in a complex medium, but also shows potential for biocompatibility as indicated by cellular assays. By utilizing the rotational motion of a stimuli-responsive DNA-based i-motif, combined with an FDA approved CA, this biocompatible platform presents an unparalleled opportunity to develop bioresponsive CAs for *in vivo* translation with ease of synthesis and tunability.

Author contributions

We strongly encourage authors to include author contributions and recommend using CRediT for standardised contribution descriptions. Please refer to our general author guidelines for more information about authorship.

Conflicts of interest

There are no conflicts to declare.

Acknowledgements

The authors would like to thank Dr. Guoxin Rong at the Institute for Chemical Imaging of Living Systems (RRID: SCR_022681) at Northeastern University for MRI imaging

support. The authors would like to thank Dr. Isen Andrew C. Calderon for assistance in carrying out preliminary studies, for helpful discussions regarding experimental design and data analysis. This work was supported by the US National Institute of Health, NINDS (1UF1NS107713-01).

Notes and references

1 B. B. Bartelle, A. Barandov and A. Jasanoff, *Neuroscience*, 2016, **36**, 4139–4148.
2 M. P. Lowe, D. Parker, O. Reany, S. Aime, M. Botta, G. Castellano, E. Gianolio and R. Pagliarin, *J. Am. Chem. Soc.*, 2001, **123**, 7601–7609.
3 R. A. Moats, S. E. Fraser and T. J. Meade, *Angew. Chem., Int. Ed. Engl.*, 1997, **36**, 726–728.
4 A. Y. Louie, M. M. Hüber, E. T. Ahrens, U. Rothbächer, R. Moats, R. E. Jacobs, S. E. Fraser and T. J. Meade, *Nat. Biotechnol.*, 2000, **18**, 321–325.
5 J. L. Major, G. Parigi, C. Luchinat and T. J. Meade, *Proc. Natl. Acad. Sci. U. S. A.*, 2007, **104**, 13881–13886.
6 A. Mishra, P. Fousková, G. Angelovski, E. Balogh, A. K. Mishra, N. K. Logothetis and É. Tóth, *Inorg. Chem.*, 2008, 1370–1381.
7 A. Mishra, N. K. Logothetis and D. Parker, *Chem. – Eur. J.*, 2011, **17**, 1529–1537.
8 G. Angelovski, P. Fouskova, I. Mamedov, S. Canals, E. Toth and N. K. Logothetis, *ChemBioChem*, 2008, **9**, 1729–1734.
9 E. L. Que and C. J. Chang, *J. Am. Chem. Soc.*, 2006, **128**, 15942–15943.
10 E. L. Que, E. Gianolio, S. L. Baker, A. P. Wong, S. Aime and C. J. Chang, *J. Am. Chem. Soc.*, 2009, **131**, 8527–8536.
11 W.-S. Li, J. Luo and Z.-N. Chen, *Dalton Trans.*, 2011, **40**, 484–488.
12 M. Andrews, A. J. Amoroso, L. P. Harding and S. J. Pope, Responsive, *Dalton Trans.*, 2010, **39**, 3407–3411.
13 S. Zhang, K. Wu and A. D. Sherry, *Angew. Chem., Int. Ed.*, 1999, **38**, 3192–3194.
14 C. Tu, R. Nagao and A. Y. Louie, *Angew. Chem.*, 2009, **121**, 6669–6673.
15 C. Tu, E. A. Osborne and A. Y. Louie, *Tetrahedron*, 2009, **65**, 1241–1246.
16 M. Polasek and P. Caravan, *Inorg. Chem.*, 2013, **52**, 4084–4096.
17 J. Wahsner, E. M. Gale, A. Rodríguez-Rodríguez and P. Caravan, *Chem. Rev.*, 2019, **119**, 957–1057.
18 P. Caravan, C. T. Farrar, L. Frullano and R. Uppal, *Contrast Media Mol. Imaging*, 2009, **4**, 89–100.
19 Y. Luo, E. H. Kim, C. A. Flask and H. A. Clark, *ACS Nano*, 2018, **12**, 5761–5773.
20 M. Woods, G. E. Kiefer, S. Bott, A. Castillo-Muzquiz, C. Eshelbrenner, L. Michaudet, K. McMillan, S. D. Mudigunda, D. Ogrin and G. Tircsó, *J. Am. Chem. Soc.*, 2004, **126**, 9248–9256.
21 H. Seo, K. Y. Ma, E. E. Tuttle, I. A. C. Calderon, A. D. Buskermolen, C. A. Flask and H. A. Clark, *ACS Sens.*, 2021, **6**, 727–732.
22 K. Gehring, J.-L. Leroy and M. Guéron, *Nature*, 1993, **363**, 561–565.
23 Y. Zhao, Z.-X. Zeng, Z.-Y. Kan, Y.-H. Hao and Z. Tan, *ChemBioChem*, 2005, **6**, 1957–1960.
24 L. Lannes, S. Halder, Y. Krishnan and H. Schwalbe, *ChemBioChem*, 2015, **16**, 1647–1656.
25 H. D. Hill, J. E. Millstone, M. J. Banholzer and C. A. Mirkin, *ACS Nano*, 2009, **3**, 418–424.
26 S. J. Hurst, A. K. R. Lytton-Jean and C. A. Mirkin, Maximizing DNA Loading on a Range of Gold Nanoparticle Sizes, *Anal. Chem.*, 2006, **78**, 8313–8318.
27 Y. Li, H. J. Schluesener and S. Xu, *Gold Bull.*, 2010, **43**, 29–41.
28 O. Edogun, N. H. Nguyen and M. Halim, *Anal. Bioanal. Chem.*, 2016, **408**, 4121–4131.
29 M. Anderson, A. Moshnikova, D. M. Engelman, Y. K. Reshetnyak and O. A. Andreev, *Proc. Natl. Acad. Sci. U. S. A.*, 2016, **113**, 8177–8181.
30 F. E. Díaz, E. Dantas and J. Geffner, *Mediators Inflammation*, 2018, **2018**, 1218297.
31 J.-H. Oh and J.-S. Lee, *Anal. Chem.*, 2011, **83**, 7364–7370.
32 D. Zanchet, C. M. Micheel, W. J. Parak, D. Gerion, S. C. Williams and A. P. Alivisatos, *J. Phys. Chem. B*, 2002, **106**, 11758–11763.
33 H. Yang, Z. Chen, L. Zhang, W.-Y. Yung, K. C.-F. Leung, H. Y. E. Chan and C. H. J. Choi, *Small*, 2016, **12**, 5178–5189.
34 X. Wu, A. C. Dawsey, B. N. Siriwardena-Mahanama, M. J. Allen and T. J. Williams, *J. Fluorine Chem.*, 2014, **168**, 177–183.
35 J. Huang, S. Gambietz and B. Saccà, *Small*, 2022, 2202253.
36 K. Malzahn, S. Ebert, I. Schlegel, O. Neudert, M. Wagner, G. Schütz, A. Ide, F. Roohi, K. Münnemann, D. Crespy and K. Landfester, *Adv. Healthcare Mater.*, 2016, **5**, 567–574.
37 C. H. Huang and A. Tsourkas, *Curr. Top. Med. Chem.*, 2013, **13**, 411–421.
38 S. Avedano, L. Tei, A. Lombardi, G. B. Giovenzana, S. Aime, D. Longo and M. Botta, *Chem. Commun.*, 2007, 4726–4728.
39 G. E. Hagberg and K. Scheffler, *Contrast Media Mol. Imaging*, 2013, **8**, 456–465.
40 K. P. Steckiewicz, E. Barcinska, A. Malankowska, A. Zauszkiewicz-Pawlak, G. Nowaczyk, A. Zaleska-Medynska and I. Inkielewicz-Stepniak, *J. Mater. Sci.: Mater. Med.*, 2019, **30**, 22.
41 M. Rohrer, H. Bauer, J. Mintorovitch, M. Requardt and H.-J. Weinmann, *Invest. Radiol.*, 2005, **40**, 715–724.
42 S. Surana, J. M. Bhat, S. P. Koushika and Y. Krishnan, *Nat. Commun.*, 2011, **2**, 340.
43 N. I. Langlois, K. Y. Ma and H. A. Clark, *Appl. Phys. Rev.*, 2023, **10**, 011304.
44 C. E. Anderson, S. B. Donnola, Y. Jiang, J. Batesole, R. Darrah, M. L. Drumm, S. M. Brady-Kalnay, N. F. Steinmetz, X. Yu, M. A. Griswold and C. A. Flask, *Sci. Rep.*, 2017, **7**, 8431.
45 G. Gambino, T. Gambino, R. Pohmann and G. Angelovski, *Chem. Commun.*, 2020, **56**, 3492–3495.

46 G. Thomas, J. Boudon, L. Maurizi, M. Moreau, P. Walker, I. Severin, A. Oudot, C. Goze, S. Poty, J.-M. Vrigneaud, F. Demoisson, F. Denat, F. Brunotte and N. Millot, *ACS Omega*, 2019, **4**, 2637–2648.